

# Deformation Monitoring and Evaluation of Mountain Slope Stability Combined With Ground-based Radar and Spaceborne InSAR Methods

Yanchao Wang (✉ [2319259348@qq.com](mailto:2319259348@qq.com))

National Institute of Natural Hazards: Institute of Crustal Dynamics <https://orcid.org/0000-0002-6187-7514>

Wenliang Jiang

National Institute of Natural Hazards: Institute of Crustal Dynamics

Bingquan Li

National Institute of Natural Hazards: Institute of Crustal Dynamics

Yi Luo

National Institute of Natural Hazards: Institute of Crustal Dynamics

Yongsheng Li

National Institute of Natural Hazards: Institute of Crustal Dynamics

---

## Research Article

**Keywords:** ground-based radar, spaceborne InSAR, deformation monitoring, slope stability, time series InSAR

**Posted Date:** June 1st, 2021

**DOI:** <https://doi.org/10.21203/rs.3.rs-555768/v1>

**License:**  This work is licensed under a Creative Commons Attribution 4.0 International License.

[Read Full License](#)

---

1           **Deformation monitoring and evaluation of mountain slope stability**  
2           **combined with ground-based radar and spaceborne InSAR methods**

3           **Author information**

4           Yanchao Wang, Wenliang Jiang, Bingquan Li, Yi Luo, Yongsheng Li  
5           National Institute of Natural Hazards, Ministry of Emergency Management of the  
6           People's Republic of China, Beijing, 100085, China  
7           Correspondence: Wenliang Jiang (jiang\_wenliang@163.com)

8           **Abstract**

9           In this paper, ground-based radar and spaceborne Interferometric Synthetic  
10          Aperture Radar (InSAR) images were combined to monitor slope stability and  
11          analyze the main deformation factors of an ancient landslide on the right bank of the  
12          Dajinchuan River in Danba County, Sichuan Province, China. We applied the short  
13          baseline set (SBAS) time series strategy with 656 scenes of ground-based radar  
14          between September 13-17, 2019, and 62 scenes of Sentinel-1 data from July 2018 to  
15          October 2020. Combined with high-resolution satellite images and digital elevation  
16          model (DEM) data, we acquired trace and quantitative deformation features and  
17          discussed the factors that contributed to slope instability, such as geological structure,  
18          topography, external environment and human activities. The largest deformation area  
19          detected by ground-based radar is located in the bedrock above the target area with a  
20          maximum cumulative deformation of more than 30 mm during the detection time. The  
21          maximum average annual deformation rate detected over the region by spaceborne  
22          InSAR is over 40 mm/a. We analyzed the differences between the ground-based radar  
23          and spaceborne InSAR and the reasons for the differences. This study provides  
24          references and suggestions for investigating potential landslide risks by combining  
25          ground-based radar and spaceborne InSAR technology.

26          **Keywords**

27          ground-based radar; spaceborne InSAR; deformation monitoring; slope stability;  
28          time series InSAR

29       **Declarations**

30       **Funding**

31           This work was financially supported by Research Grants from the National  
32 Institute of Natural Hazards, MEMC, (grant numbers ZDJ2019-17 and ZDJ2020-04),  
33 and the National Natural Science Foundation of China (41772219).

34       **Conflicts of interest/Competing interests**

35           The authors have no financial or proprietary interests in any material discussed in  
36 this article.

37       **Availability of data and material**

38           The sentinel-1 data and regional geological data can be downloaded from  
39 Internet, the ground-based radar cannot be deposited.

40       **Code availability (Not applicable)**

41       **Authors' contributions**

42           All authors contributed to the study conception and design. Material preparation,  
43 data collection and analysis were performed by Yanchao Wang, Wenliang Jiang,  
44 Yongsheng Li. The ground-based radar data was collected by Bingquan Li and Yi Luo.  
45 The first draft of the manuscript was written by Yanchao Wang and all authors  
46 commented on previous versions of the manuscript. All authors read and approved the  
47 final manuscript.

48       **Ethics approval**

49           No conflict of interest exists in the submission of this manuscript, and manuscript  
50 is approved by all authors for publication. I would like to declare on behalf of my  
51 co-authors that the work described was original research that has not been published  
52 previously, and not under consideration for publication elsewhere, in whole or in part.  
53 All the authors listed have approved the manuscript that is enclosed.

54       **Consent to participate**

55           It has been approved by all co-authors.

56       **Consent for publication**

57           This manuscript's publication has been approved by all co-authors.

## 58 **1. Introduction**

59 China is among the countries with the most serious geological disasters in the  
60 world. Unfortunately, accurately predicting and warning about geological hazards are  
61 challenging tasks (Hongqi Chen et al. 2011). At present, more than 300,000 hidden  
62 geological hazards have been found in China, but nearly 70% of the major geological  
63 disasters that have occurred in recent years were not found within the scope of these  
64 hidden hazards, and a large number of hidden hazards have not been found (Xu 2020).  
65 Landslides are one of the most important geological disasters, and they not only  
66 threaten human lives but also seriously damage the environment, resources and  
67 property. With the sustained and rapid development of the national economy,  
68 large-scale projects, such as urbanization, railways and hydropower projects, have been  
69 developing in depth. For example, the construction of the Sichuan-Tibet Railway and  
70 the Baihetan Dam will greatly transform the engineering geological conditions.  
71 Therefore, an increasing number of construction projects and engineering projects will  
72 be exposed to increased geological hazards, which will increase the disaster risk level.  
73 On the other hand, the aggravation of global warming and climate change in recent  
74 years has led to an increase in “warming and wetting” of the Tibetan Plateau (Duan et al.  
75 2016), and the influence of major natural disasters and disaster chains will become  
76 more significant. In addition, because transformation and destruction of the natural  
77 environment caused by human disturbance are better, the balance of the natural  
78 environment has changed, and the deterioration of the natural environment will  
79 eventually feedback to human society. Therefore, it is of great significance to  
80 strengthen the identification and dynamic monitoring of geological hazards to achieve  
81 advanced risk perception, early warning and accurate emergency response of  
82 geological hazards. Thus, precedures are necessary and important guarantees to reduce  
83 the casualties and economic losses caused by geological hazards.

84 Recently, the rapid development of sky-ground multiplatform measurement  
85 technology has provided important technical means for risk assessment, early warning  
86 and emergency monitoring of geological hazards. Many scholars have carried out a

87 large number of studies on the early identification and dynamic monitoring of  
88 geological hazards (Casagli et al. 2017; Lu Zhang et al. 2018; Lu et al. 2019). Among  
89 these platforms, optical satellites and InSAR satellites are the most widely used at  
90 present. However, the role of spaceborne technology is more focused on the early  
91 identification of geological hazards. In the field of unmanned aerial vehicles, aerial  
92 photogrammetry plays an important role in high-precision geological hazard surveys  
93 and emergency observations due to its flexibility and relatively low cost. In addition,  
94 ground-based radar technology has also been an important supplement to  
95 ground-based observation technology, which can carry out long-distance and  
96 high-precision observations of major geological hazards; therefore, it is very  
97 important to avoid in situ instrument deployment for monitoring and early warnings  
98 of major geological hazards and emergency observations (Luo et al. 2020). At present,  
99 the application of ground-based radar observation technology in geological hazard  
100 monitoring is still in the experimental and exploration stage.

101 In this study, the mountain slope stability of an ancient landslide on the right  
102 bank of the Dajinchuan River in Danba County, Sichuan Province, China, is  
103 monitored by ground-based radar and spaceborne InSAR methods. Combined with  
104 high-resolution image and DEM data, we study the trace features and quantitative  
105 deformation features of the ancient landslide. The influence of landform, slope  
106 direction, geological structure, river erosion, stratum rock group and human activity  
107 on the hidden hazards are also analyzed. At the same time, the difference and  
108 relationship between the ground-based radar and spaceborne InSAR are analyzed and  
109 compared, and the main factors that cause the differences are discussed. This study  
110 will provide references and suggestions for monitoring the hidden danger of  
111 geological hazards by combining ground-based radar and spaceborne InSAR  
112 technology.

## 113 **2. Study area description**

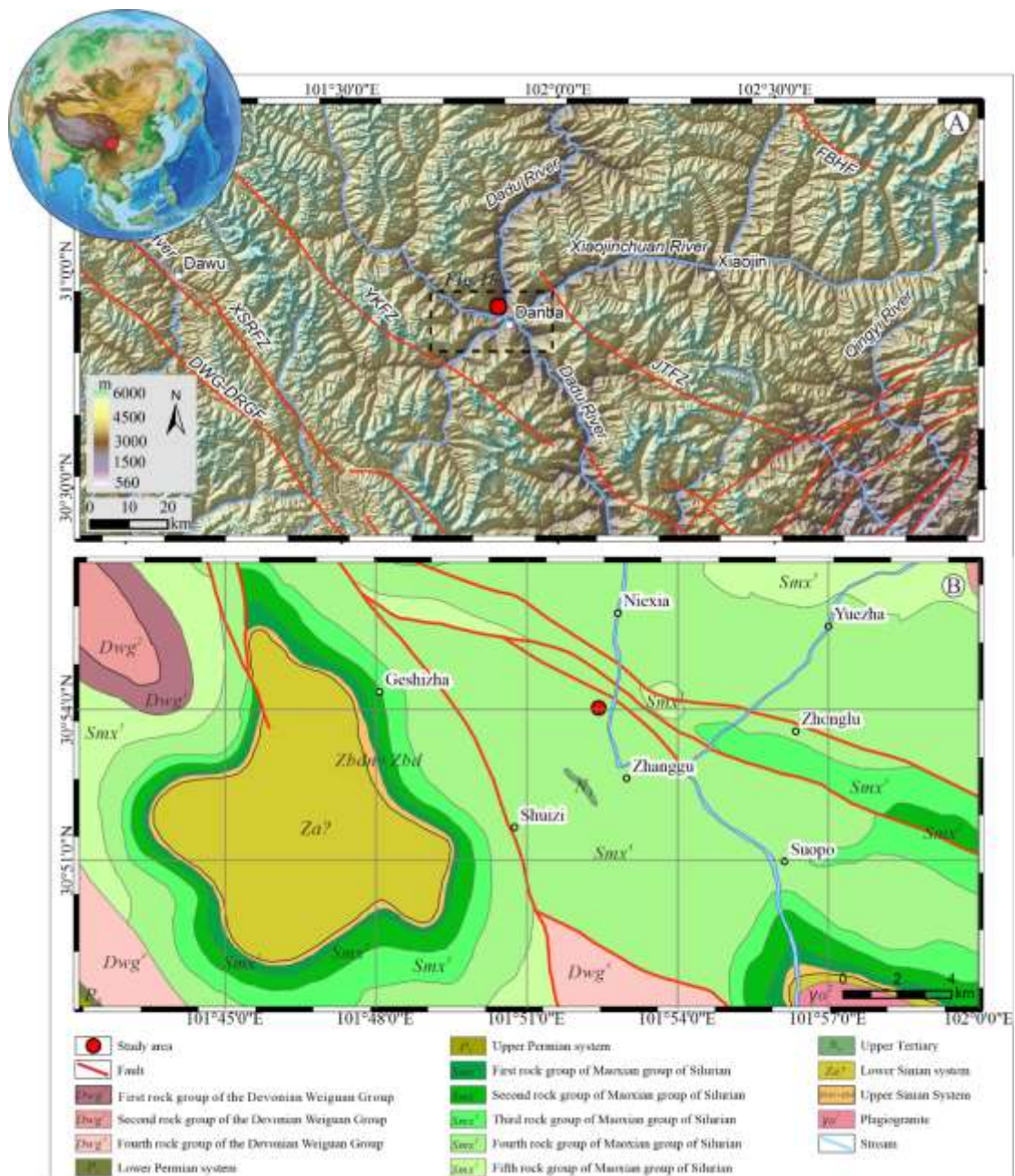
114 The study area is located in Jiaju village, Danba County, Sichuan Province. Danba  
115 County is located from the first to second step of the topographic transition zone in

116 China, where the terrain is extremely complex and significantly characterized by an  
117 alpine canyon landform. The Dadu River cuts across Danba County from north to south  
118 (Fig 1), with river channels of 1000 to 3000 m in depth. In contrast, influenced by the  
119 high mountain and canyon topography, Danba County is characterized by the Tibetan  
120 Plateau monsoon. Moreover, the area is also characterized by obvious vertical zonality  
121 due to topographic factors. With increasing altitude, both the temperature and  
122 evaporation decrease gradually; however, the precipitation increases. The precipitation  
123 is mainly concentrated between May and September, the rainy season and dry season  
124 are obviously different, and the temperature varies greatly from day to night.

125 Danba County is situated in the contact zone of several tectonic blocks, including  
126 the Bayankara block and Sichuan-Yunnan rhombic block. Under the action of several  
127 phases of mountain building and metamorphism, the geological structures are  
128 extremely complicated, with diversified folding structures and interlaced fault  
129 structures trending NW. The complex lithologies are mainly metamorphic rocks, and  
130 the strata are relatively complete with only a few missing strata (Nie 2018). Geological  
131 disasters occur frequently in Danba County and are characterized by sudden occurrence,  
132 strong concealment, and significant damage (Minghui Li et al. 2008). With the increase  
133 in construction projects, especially the multistage water-power engineering projects in  
134 the Dadu River, geological disasters in this region are becoming increasingly serious,  
135 and many old landslides have been reactivated.

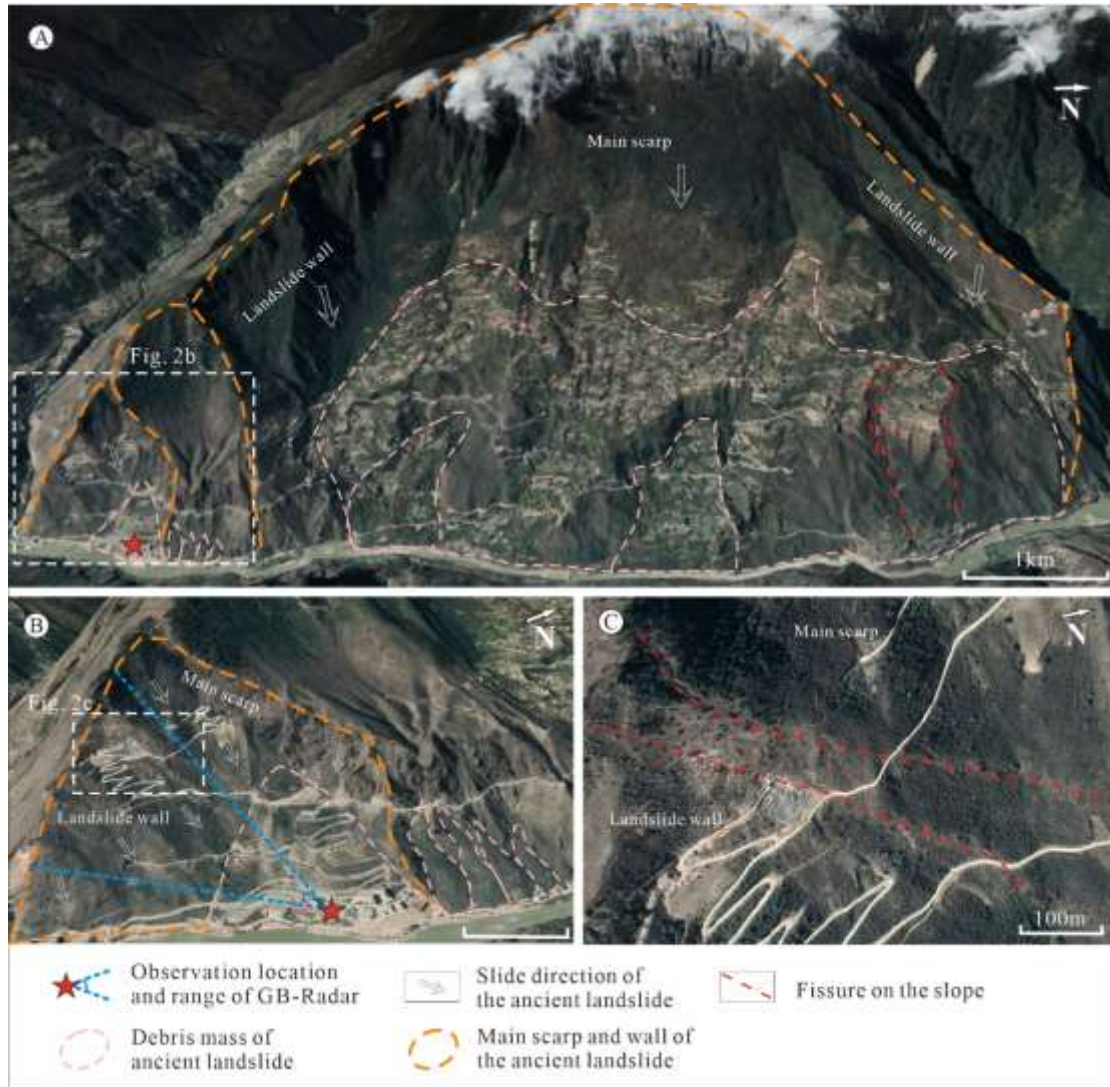
136 The study area of this paper is located on the right bank of the Dajinchuan River  
137 (Fig 2), a tributary of the Dadu River. The study area is also situated at the foot of the  
138 right front slope of the old, large Jiaju landslide group, which consists of many  
139 secondary landslides that led to multiple bank deformation events along the  
140 Dajinchuan River. The observation area of the ground-based radar in this study is the  
141 slope bedrock of a secondary ancient landslide. The front edge of the ancient landslide  
142 is approximately 1.4 km in length, and the height difference between the front and back  
143 edges of the landslide is more than 700 meters. The general terrain slope exceeds 25  
144 degrees according to the DEM data. Two rock fractures extending in the northeast

145 direction can be clearly interpreted from the Google Earth images in the observation  
 146 area of the ground-based radar (Fig 2(c)). The upper fracture is approximately 820 m in  
 147 length, and the lower fracture is approximately 600 m in length. To study the  
 148 deformation feature of this bedrock slope of the ancient landslide, we utilized  
 149 ground-based radar and the satellite InSAR method. The deformation results measured  
 150 by the two methods are analyzed, and these results may help to better understand the  
 151 landslide in similar studies.



152  
 153 Fig 1(a) Regional hillshade map of the study area. A Shuttle Radar Topography Mission (SRTM)  
 154 hillshade map is used as the base map. (b) Regional geological setting surrounding the study area

155 (China Geological Survey, 2014). The red line denotes the main faults in this region. YKFZ: Yuke  
 156 fault zone; JTFZ: Jintang arc fault; XSHFZ: Xianshui River fault; DWG-GRGF:  
 157 Dawagou-Dourigou fault; and FBHF: Fubian River fault.



158  
 159 Fig 2 Geographic location map. (a) The whole picture of the Jiayu landslide group. (b) The location  
 160 and range of ground-based radar. (c) The surface fissure on the slope.

161 **3. Data and methods**

162 **3.1 Measurement principle of ground-based radar**

163 The ground-based radar data used in this study are acquired by the portable radar  
 164 interferometer GPRI-II (Gamma Portable Radar Interferometer) produced by GAMMA  
 165 company. This interferometer uses real aperture radar with a radar frequency of 17.2  
 166 GHz (Ku band), bandwidth of 200 MHz, wavelength of 0.0176 m and effective

167 measurement range from 0.05 to 10 km. The deformation monitoring accuracy can  
 168 reach the submillimeter level with an azimuth resolution of 6.28 m (when the distance  
 169 is 1 km) and a range resolution of 0.75 m. The GPRI-II is mounted on a tripod and  
 170 measured at 360° by a rotating scanner with three antennas, one transmitting signal and  
 171 two receiving the echo signal.

172 GPRI-II uses a frequency-modulated continuous wave (FMCW) to measure the  
 173 velocity and distance of the target by the frequency differences between the transmitted  
 174 signal and received signal. This technique is suitable for data acquisition and digital  
 175 signal processing with low difference frequency signals and simple hardware  
 176 processing. Compared with SFCW (step frequency continuous wave), GPRI-II can  
 177 improve the scanning speed and reduce the influence of the atmospheric delay phase on  
 178 the monitoring precision, reducing the phase distortion caused by system noise in the  
 179 long-term scanning process. At the same time, GPRI-II can generate a DEM by means  
 180 of two antennas. The system generally uses the continuous observation mode to  
 181 continuously observe the target area.

182 The range resolution of GPRI-II is

$$183 \quad \Delta d_{sr} = \frac{c}{2B}$$

184 where C is the speed of light and B is the bandwidth. As seen from the above  
 185 equation, the range resolution is independent of the distance between the instrument  
 186 and the observed target.

187 The azimuth resolution is

$$188 \quad \Delta d_{az} = \sin(\theta_{-3dB}) \cdot R$$

189  $\theta_{-3dB}$  is the width of the half-power wave velocity, and R is the azimuth distance.

190 Since the spatial baseline of GPRI-II is 0 and the observation mode is continuous,  
 191 the interferometric phase of GPRI-II does not include the terrain phase and the  
 192 geometric phase component between the two positions; thus, the interferometric phase  
 193 is

$$194 \quad \Delta\varphi = \varphi_{defo} + \varphi_{atmo} + \varphi_{noise} + 2k\pi$$

195 In the formula,  $\varphi_{defo}$  is the deformation phase,  $\varphi_{atmo}$  is the atmospheric delay

196 phase, and  $\varphi_{noise}$  is the noise phase.

197 Compared with the spaceborne InSAR system, the ground-based radar system  
198 has several unique advantages (Wu et al. 2019; Tiandong Chen 2020). First, the  
199 precision of the ground-based radar is higher up to the submillimeter level as its  
200 wavelength is shorter. Second, the observation period of ground-based radar is shorter,  
201 and the time sampling rate is higher to simplify the phase unwrapping process and  
202 achieve rapid real-time monitoring. Third, the ground-based radar system is more  
203 portable and flexible because it can be monitored at any time according to the  
204 conditions of the disaster, and the observation angle and observation time interval can  
205 be adjusted, making it more suitable for slope deformation monitoring. Finally, the  
206 ground-based radar installed on the observation station has no influence on the space  
207 baseline or orbit error.

### 208 **3.2 Ground-based radar data acquisition**

209 To obtain the echo signal as much as possible and ensure the stability of the  
210 platform, the set-up position of GPRI-II should consider the following four conditions  
211 (Bingquan Li et al. 2019). The first is good visibility, and the equipment should be set  
212 up in a position with high visibility and no obstacles between the equipment and target  
213 area. Second, a reasonable observation distance, that is, the appropriate monitoring  
214 distance, should be selected according to the actual situation of the site, such as the  
215 topography, engineering, hydrology and other conditions. The larger the distance is, the  
216 weaker the radar receiving echo signal, and the worse the monitoring effect. The third  
217 condition is that the equipment should be placed on a stable observation platform to  
218 reduce the influence of any small equipment movement on the observation accuracy.  
219 The last condition is a suitable viewing angle. The smaller the angle is, the more  
220 sensitive the radar is to the intensity of the deformation signal, but it is disadvantageous  
221 to receive the echo signal. In ground-based radar deformation monitoring, the  
222 observation parameters should be adjusted at the beginning according to the  
223 environmental factors and the quality of the observation data because the subsequent  
224 data processing accuracy has a great impact.

225 In this study, the instrument was set up in the Jiajuzangzhai tourist center in a  
 226 continuous observation mode. The monitoring time was from 8:27 to 21:37 on  
 227 September 13, 2019, and from 16:46 on September 15 to 13:26 on September 17, 2019.  
 228 The time interval between the two receiving antennas was approximately 10 minutes  
 229 and one scene, and the total number of images was 656 scenes. The observed  
 230 parameters are shown in Table 1.

231 Table 1 Measured parameters of the ground-based radar

<b>Index</b>	<b>Parameter</b>
Platform location	101.878°E, 30.905°N
Platform elevation	1927.3 m
Measurement range	0.45-1.3 km
<b>Coherence threshold</b>	0.35
<b>Antenna-pitch</b>	20°
<b>Azimuth</b>	229.3°

232

### 233 3.3 Data processing flow

234 GPRI-II ground-based radar and spaceborne InSAR have basically the same time  
 235 series analysis process; the largest difference is that the ground-based radar spatial  
 236 baseline is 0, without image registration and terrain phase compensation. The  
 237 processing flow of ground-based radar data mainly includes data preprocessing,  
 238 interference processing, coherent point extraction, phase filtering, phase unwrapping,  
 239 atmospheric correction, time series analysis and geocoding (Wang et al. 2019a; Wang et  
 240 al. 2019b).

241 During the process of coherent point extraction, an adequate number of high  
 242 quality coherent points are very important to the precision of deformation monitoring  
 243 results. The methods of coherence point extraction mainly include the amplitude  
 244 departure threshold method, local coherence method (coherence coefficient threshold

245 method) and nonlocal method. In this paper, a nonlocal method is used to extract  
246 coherent points by selecting homogeneous or similar pixel estimates from the  
247 surroundings of each resolution unit.

248 In the process of phase unwrapping, there is a  $2k\pi$  relation between the initial  
249 phase and the true phase in the interferogram. The initial phase is the winding phase  
250 between  $-\pi$  and  $\pi$ , which is the main value of the true phase. The interference phase  
251 needs to be decoded to obtain the true phase. Considering the stability and time effect  
252 of phase unwrapping, the three-dimensional phase unwrapping method is adopted in  
253 this paper.

254 Atmospheric correction is also necessary for ground-based radar data (Xining  
255 Zhang et al. 2017). Ground-based radar relies on the phase information of radar signals  
256 for ranging, but the accuracy of ranging is affected by the changes in the refractive  
257 index of the radar signals because of the atmosphere. Even for short-term monitoring,  
258 shortwave band ground-based radar is also very sensitive to weather changes, so  
259 improving the measurement error caused by atmospheric phases has become the key  
260 technology to improve the observation accuracy of ground-based radar. In this paper, an  
261 iterative decomposition model is used to correct the effect of atmospheric variations on  
262 the deformation results.

263 We use the singular value decomposition method (Li et al. 2013) to generate the  
264 deformation time series diagram. The deformation characteristics, including the spatial  
265 distribution, deformation intensity and future development trend, can be estimated by  
266 the time series map of deformation, which provides a basis for emergency response.

### 267 **3.4 Other auxiliary data**

268 To investigate the features of the slope, as well as for comparison with the  
269 deformation results obtained by ground-based radar GPRI-II, remote sensing data from  
270 different platforms were also employed, including spaceborne InSAR and  
271 high-resolution Google Earth images. A total of 62 scenes of Sentinel-1 data from July  
272 2018 to October 2020 were selected for deformation analysis.

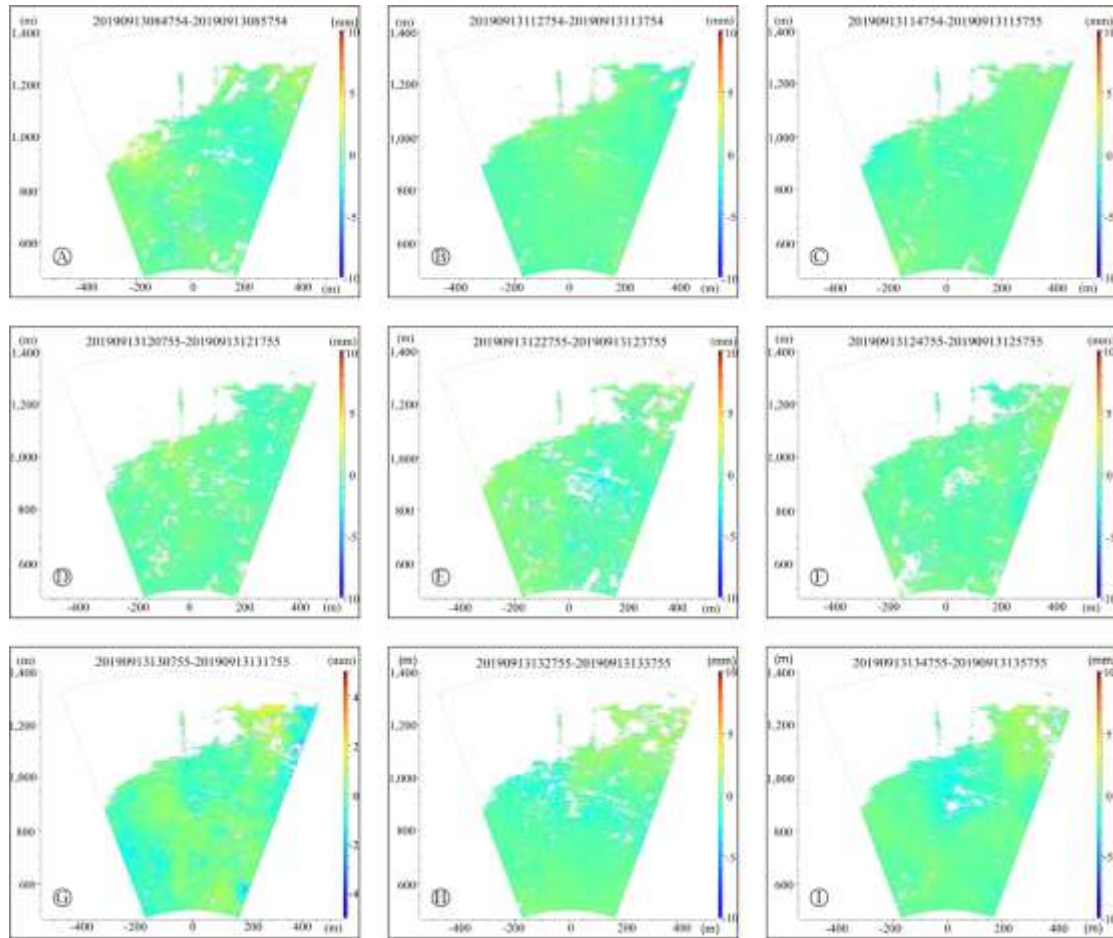
273 Other auxiliary data, including geological maps and meteorological and

274 hydrological data, were also employed in the study.

## 275 **4. Results and analyses**

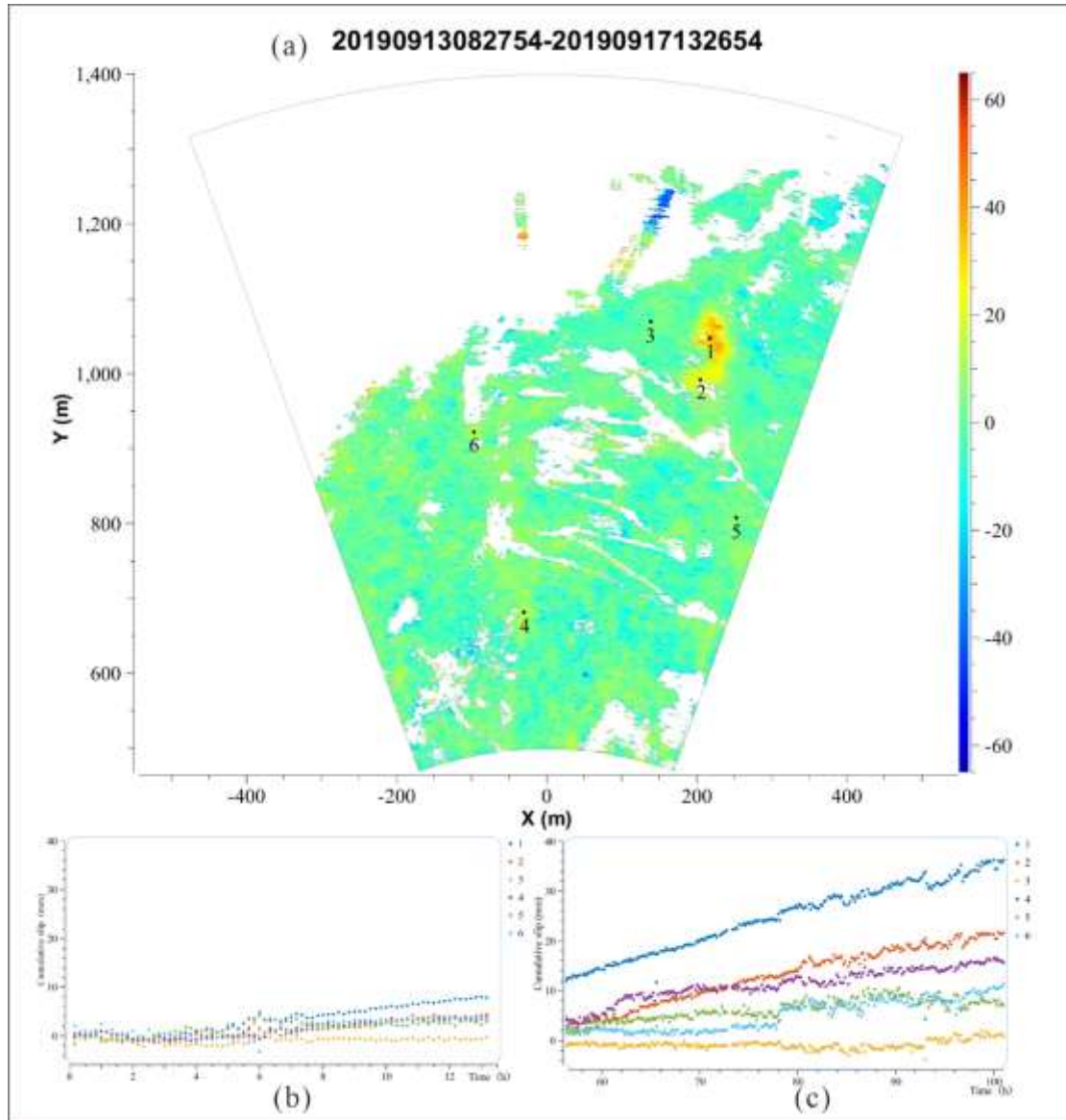
### 276 **4.1 Deformation results of ground-based radar**

277 The effective monitoring time of ground-based radar is from 8:27 on 13  
278 September to 21:37 on 13 September and from 16:46 on 15 September to 13:26 on 17  
279 September. The maximum monitoring distance is approximately 1300 m, and the  
280 minimum monitoring distance is approximately 450 m. According to the processing  
281 flow in section 3.3, we set the parameters, which include the unit window size and time  
282 baseline. Since the data format of the data acquisition system synchronized to the  
283 ground-based radar data processing system is binary, it needs to be converted to MAT  
284 format. The average coherence criterion is used to extract the coherent points, and the  
285 nonlocal coherence algorithm is used to set the coherence threshold value to 0.35, the  
286 nonlocal window to 15, the similarity threshold value to 0.9, the minimum similarity  
287 point to 10, and the maximum similarity point to 45. Some of the differential  
288 interferograms produced during ground-based radar data processing are shown in Fig 3.  
289 The numbers at the top of each figure represent the observation dates of the two data  
290 points used to generate the differential interferograms. As shown in Fig 4, there is  
291 obvious deformation in the monitoring area. The main deformation area is above the  
292 continuous curve. The maximum cumulative deformation is more than 30 mm.



293

294 Fig 2 Examples of differential interferograms generated during the processing of ground-based  
 295 radar data. The two numbers in the upper part of each figure denote the observation dates of two  
 296 data points used to generate the differential interferogram. 20190913084754-20190913085754  
 297 denotes the differential interferogram generated between two data points observed at 8 h 47 m 54 s  
 298 on September 13, 2019, and at 8 h 57 m 54 s on September 13, 2019. The origin point of the  
 299 coordinate system is the position of the ground-based radar.



300

301 Fig 4 (a) Cumulative slips of the slope deformation along the LOS direction measured by the  
 302 ground-based radar device. The number at the top of the figure represents the time when  
 303 ground-based radar began and ended observations, that is, the observation time range of the  
 304 cumulative deformation map generated; and 20190913082754-20190917132654 represents  
 305 ground-based radar observation time from 8:27:54 on September 13, 2019 to 13:26:54 on  
 306 September 17, 2019. The origin of the coordinates represents the position of the ground-based  
 307 radar. (b) and (c) are the results of the accumulated deformation of the selected points in the time series  
 308 of 0~13.5 h and 56~101 h, respectively.

309

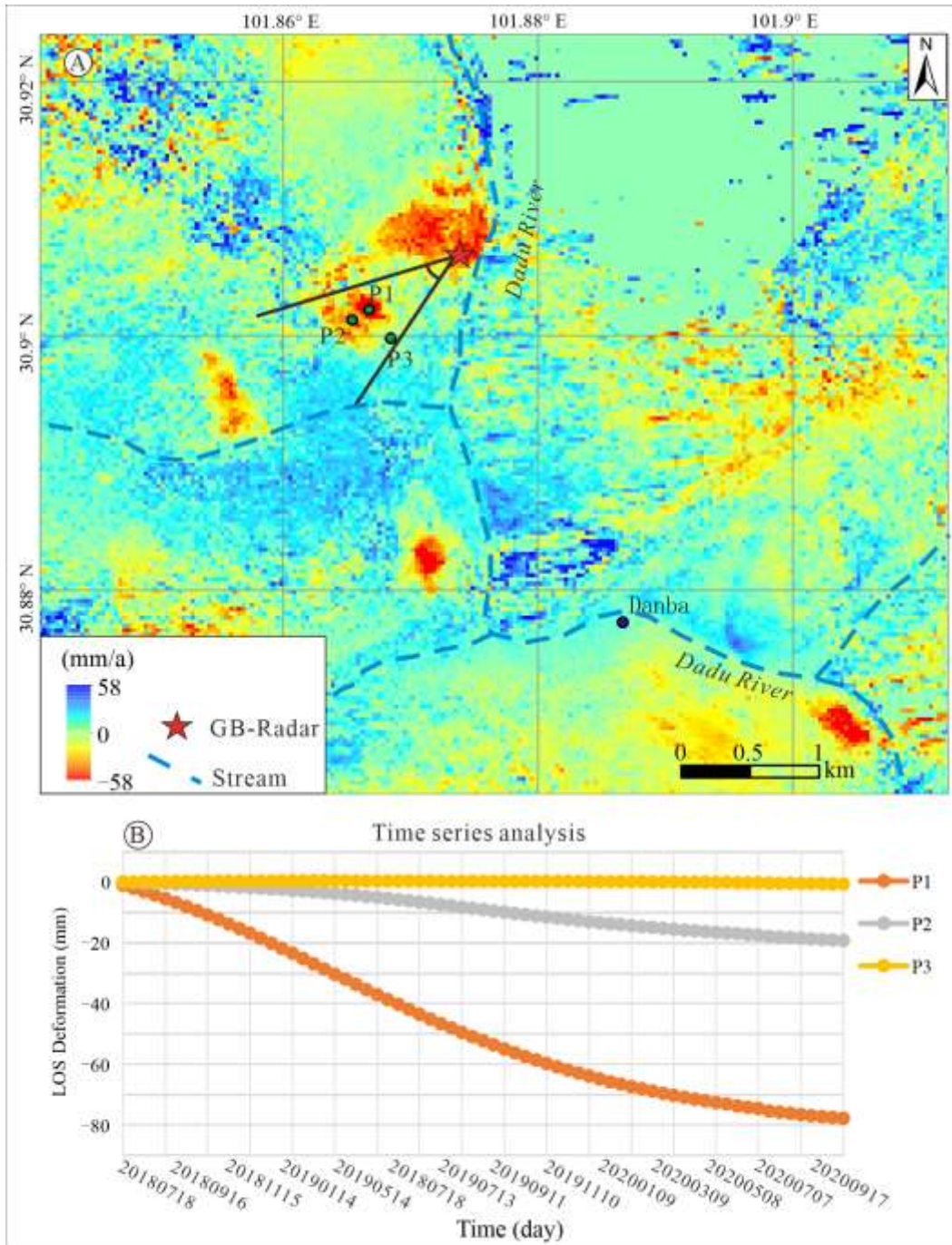
#### 4.2 Deformation results from spaceborne InSAR

310

Sixty-two scenes of Sentinel-I downorbiting data covering the study area from

311 July 2018 to October 2020 were processed using GAMMA software, and the average  
312 annual deformation rate of the study area over this period was obtained using the short  
313 baseline set (SBAS) processing method (Fig 5(a))(Yongsheng Li et al. 2013). The  
314 maximum average annual deformation rate in the region is over 40 mm/a. The main  
315 deformation areas monitored are located along the banks of the Dadu River and its  
316 tributary, the Dajinchuan River. These deformation areas all have different degrees of  
317 human activities, such as road construction.

318 In the observation area of ground-based radar, the gray line in Fig 5(a), three  
319 points are selected for time series analysis. The result of the line-of-sight cumulative  
320 deformation is shown in Fig 5(b). The maximum cumulative deformation is  
321 approximately 80 mm, which is located in the lower part of the continuous bedrock  
322 curve of the landslide's back wall.



323

324 Fig 5(a) Regional annual deformation rate map measured by Sentinel-1 data, and P1, P2  
 325 and P3 are the three points selected in the observation area of ground-based radar. The  
 326 gray line is the scanning angular scope of ground-based radar. (b) The line-of-sight  
 327 cumulative deformation map of three selected points P1, P2 and P3 in the study area.

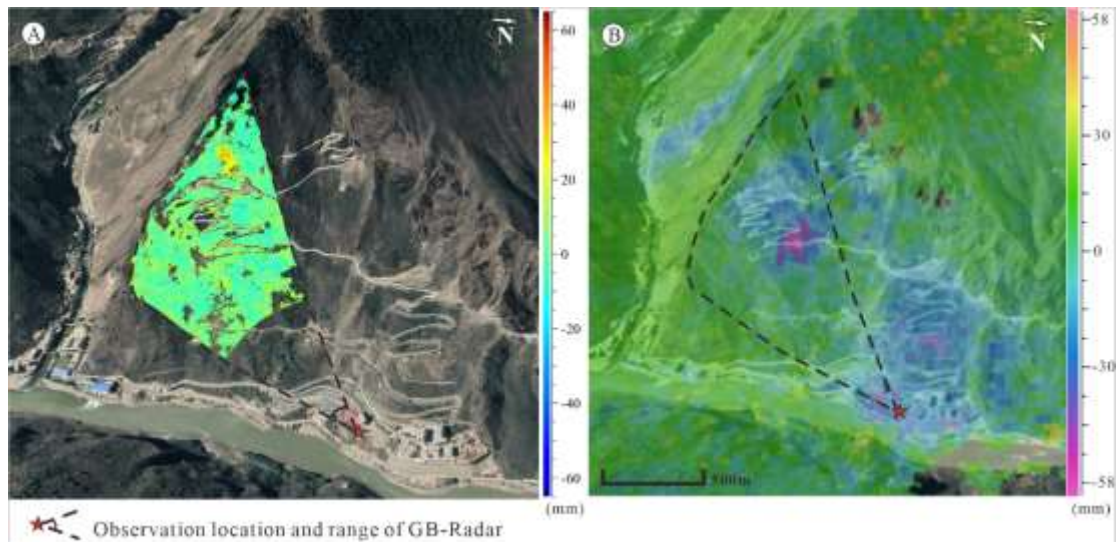
328 **5. Discussion**

## 329 **5.1 Deformation analysis of the mountain slope**

330 We match the ground-based radar and spaceborne InSAR data accurately and  
331 superpose to the Google Earth 3D image (Fig 6) to compare the image features of  
332 different deformation regions. According to the interpretation of satellite remote  
333 sensing images, the main target area of this observation is located on the right wall of a  
334 pre-existing ancient landslide. The accumulation body of the early ancient landslide is  
335 mainly located at the left foot of the ancient landslide, which is the upper part of the  
336 scenic area. Some accumulation bodies remain on the right side of the ancient landslide.  
337 The target area observed by ground-based radar is mainly on the right side of the  
338 ancient landslide, and the back wall is the blind area, which is not effectively covered.

339 By monitoring the right wall of the ancient landslide with ground-based radar,  
340 some deformation is observed in the area. The largest deformation area detected by  
341 ground-based radar is located in the bedrock above the target area. The maximum  
342 deformation area is approximately 150 m across the slope and 300 m up and down the  
343 slope. This deformation belongs to the back wall bedrock zone of the pre-existing  
344 ancient landslide body and is a push-type landslide.

345 At the same time, in the deformation map obtained by spaceborne InSAR  
346 monitoring, there is a large range of deformation in the target area, especially in the  
347 bottom and upper parts. The bottom deformation region is the left front accumulation of  
348 the pre-existing landslide body, which is the area of continuous curving road in the  
349 upper part of the scenic spot. The upper deformation region is located in the lower part  
350 of the maximum deformation region observed by ground-based radar and corresponds  
351 to the continuous curve region on the right wall of the landslide. The deformation of  
352 two continuous curved road areas is the result of road construction and can be found in  
353 the InSAR long time series result. In contrast, the maximum deformation region  
354 observed by ground-based radar reflects the effect of rainfall on slope stability due to  
355 the September flood season. The deformation in this area is at a large scale, and local  
356 periodic deformation occurs in relation to the flood season.



357  
 358 Fig 6(a) Map of ground-based radar monitoring results superimposed on Google Earth;  
 359 (b) Map of Sentinel 1 monitoring results superimposed on Google Earth.

### 360 **5.2 Main factors influencing slope deformation**

361 In general, the factors that affect the stability and deformation of geological slopes  
 362 include geological structure, topography, external environment and human activities.  
 363 Based on the observational results analysis, deformation is the result of these  
 364 abovementioned factors.

365 In terms of geological structure, Danba County lies at the intersection of three  
 366 important active tectonic belts, namely, the northwest Xianshui River Fault Zone, the  
 367 northeast Longmen Mountain thrust zone and the nearly south-north Anninghe Fault  
 368 Zone. These three fault zones are all active Holocene fault zones with important  
 369 seismogenic tectonic settings. Geological hazards in this area are prone to occur  
 370 because of strong tectonic activity and broken internal blocks under the influence of  
 371 three active tectonic belts. In addition, the block is located at the front of the Bayankara  
 372 Block and is in a strong uplift region along the Longmen Mountains tectonic belt.  
 373 Therefore, this region is characterized by high mountains and deep valleys, and rapid  
 374 and serious valley undercutting is taking place. The slope angle on the left bank of the  
 375 river is  $36^\circ$ , and the slope gradient on the right bank is more than  $30^\circ$ . Under the  
 376 influence of both the uplift of the mountain body and the deep cut of the valley, the  
 377 increase in the effective open plane formed at the front of the deformation body  
 378 increases the gravitational potential energy of the slope, leading to the decrease in the

379 stability of the slope, and creep deformation of the slope easily occurs under the action  
380 of gravity. There are cracks in the broken rock of the bedrock slopes, and rainfall can  
381 easily permeate the bedrock, which promotes slope sliding along the bedding surface  
382 and affects the stability of slopes. Therefore, strong tectonic activity is the most  
383 important factor for the development of geological hazards in Danba County.

384 In terms of topography and geomorphology, the slope angle of a geological body  
385 is an important factor that affects its stability. Generally, geological bodies with slope  
386 angles greater than 10 are subject to unstable deformation under the action of gravity  
387 (Donnarumma et al. 2013; Luo et al. 2020). According to the regional DEM, the slope  
388 angle of the whole terrain is more than 30° and the gradient is more than 0.58, while the  
389 slope angle of the local slope of ground-based radar is more than 20° and the gradient is  
390 more than 0.41 (Fig 7). Whether considering the whole terrain or the local terrain, the  
391 slope of the terrain is very large, and it easily loses stability and deforms under  
392 disturbances by internal structural factors and external artificial factors.

393 In addition, there is a gentle platform in the upper part of the observation slope,  
394 which presents as a low-slope above and steep characteristics below over the whole  
395 terrain. This topographic feature is not conducive to rapid drainage of heavy rainfall  
396 during the flood season (Luo et al. 2020). Under the condition of poor drainage at the  
397 top, the accumulated water will gradually permeate into the interior of the formation,  
398 thus acting as a lubricant in the interior of the rock formation, causing the slope to be  
399 more prone to instability and deformation under the action of gravity. This finding also  
400 shows that the deformation observed by ground-based radar in this study is mainly  
401 concentrated in the flat-top area of the platform.



Fig 7 Sketch map of the slope and angle of the study area

402

403

404 The external environmental factors are mainly hydrometeorological conditions,  
 405 erosion and weathering. Danba County is in the Tibetan Plateau monsoon climate in the  
 406 Northern Hemisphere subtropical climate zone, located in the Dadu River Valley  
 407 Watershed. Rainfall is concentrated in June-August, and the annual total precipitation  
 408 is generally 500-1000 mm. Mountain torrents and mud-rock flows frequently occur in  
 409 Danba County under the influence of heavy rainfall; for example, the Danba County  
 410 region suffered 60-year floods in June 2020 under the influence of heavy rainfall, and  
 411 several places, including Banshanmen, Donggu, and Mozigou, suffered flood debris  
 412 flows. River erosion is also very strong due to the breaking and cutting of the valley  
 413 because of the influence of heavy rainfall and strong tectonic activity. The water level  
 414 rises and falls steeply during the flood season, and the dynamic water pressure and  
 415 uplift force change rapidly in the slope. When the water level falls rapidly, the abnormal  
 416 increase in hydrodynamic pressure and the rapid decrease in uplift force play a large  
 417 role in triggering the failure of the slope, and the foot of the slope is easily cut so that the  
 418 upper rock mass loses its support, and then, the slope loses its stability.

419 In addition to the above natural factors, human activities, especially engineering  
 420 construction disturbance factors, which increase with the development of the social  
 421 economy, are also important factors affecting the stability of slopes. These effects  
 422 include engineering cut slopes and slope angles and persistent engineering disturbances.  
 423 The remote sensing images show that there is a continuous curved road in the middle of  
 424 the slope. Although the road scale is not large, this curved road has the phenomenon of

425 horizontal repeated slope cutting, and there is a large range of construction in the top  
426 platform of the observation area, which changes the slope gradient and forms the terrain  
427 characteristics mentioned above. The strong deformation area observed by ground  
428 radar is located in the upper part of the road construction area. Under the influence of  
429 the slope-cutting disturbance, two clear and continuous surface fissures were formed in  
430 the upper part of the platform, one of which was more than 900 m in length and the  
431 other was more than 600 m in length. According to remote sensing image records,  
432 roads were built from 2011 to 2012; although the scale was small, roads became one of  
433 the important factors that induced slope instability and deformation under the  
434 disturbance of long-term human activities.

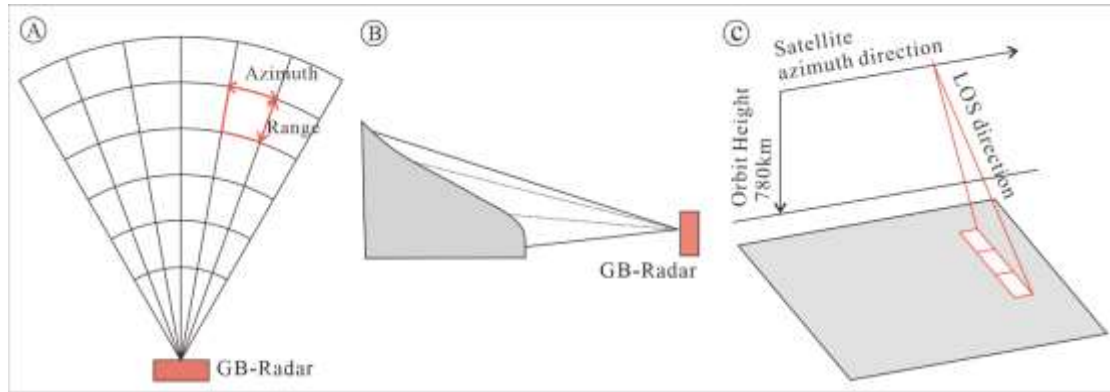
### 435 **5.3 Difference analysis of spaceborne and ground-based observation results**

436 The main reasons for the inconsistent characterization results of the deformation  
437 area between spaceborne InSAR and ground-based radar include the inconsistent time  
438 period length of satellite and ground observations, the observation mode and angle of  
439 satellite and ground surface, the difference in deformation reference points, the  
440 mismatch of image resolution and observation accuracy, and the phase difference.

441 In terms of the observation time cycle, spaceborne InSAR data were collected  
442 from July 2018 to October 2020, with a 12-day interval of 62 scenes. The ground-based  
443 radar monitoring time was from September 13 to September 17, 2020. There is a large  
444 difference in the observation time and the collection time interval between them.  
445 Spaceborne InSAR has a larger time span, longer acquisition interval, and  
446 ground-based radar has a smaller time span, shorter acquisition interval, higher time  
447 resolution and better data accuracy.

448 In terms of the difference between the observation mode and the incident angle,  
449 the ground-based radar and spaceborne InSAR monitoring schematic diagram is shown  
450 in Fig 8. Ground-based radar is installed in a flat field opposite the study area and  
451 scanned by a rotating scanner at a set angle. The elevation angle of this experiment is  
452  $20^\circ$ , and the range of radar scanning angles is  $-20^\circ\sim 20^\circ$ . Sentinel-1 data have a variety  
453 of imaging modes. The interference width mode is the default mode for land cover.

454 Progressive terrain scanning technology TOPSAR is used to obtain three subbands, and  
455 the incident angle is in the range of  $29^{\circ}\sim 46^{\circ}$ . The imaging mode and the observation  
456 angle are different, and the angle of the line-of-sight deformation is also different,  
457 which affects the observation result.



458  
459 Fig 8(a) Ground-based radar monitoring plan sketch (b) Ground-based radar  
460 monitoring profile sketch (c) A schematic of the Sentinel-1 imaging mode

461 The reference datum points of deformation are different. The base point of  
462 ground-based radar is located at the foot of the slope, so the observed deformation is  
463 closer to the real deformation characteristics of the landslide. The spaceborne InSAR  
464 data reference point is relatively stable in the whole image, which is located a large  
465 distance from the slope, so the deformation shown is also relative to other reference  
466 points. There may be overall deformation in a region that either increases or counteracts  
467 the true deformation of the slope.

468 In terms of imaging resolution and deformation monitoring accuracy, the medium  
469 resolution of the spaceborne InSAR Sentinel-1 is  $5\text{ m} \times 20\text{ m}$ , and the time series  
470 processing accuracy is at the mm level. The range resolution of the ground-based radar  
471 is  $0.75\text{ m}$ , and the azimuth resolution at  $1\text{ km}$  is  $6.8\text{ mrad}$  with submillimeter accuracy.  
472 The data precision of the ground-based radar is obviously higher than that of  
473 spaceborne data, but it is not suitable for long-term and large-scale observations, and  
474 spaceborne data are not suitable for small-scale deformation objects.

475 In data processing, the space baseline of ground-based radar is 0, there is no need  
476 for terrain phase compensation, and there is no influence from an orbit error. The  
477 influence of the atmosphere is weak due to the limited observation distance. In contrast,

478 there is not only the influence of the spatial baseline but also a large interference of  
479 atmospheric error in spaceborne InSAR data processing, so it is necessary to repeatedly  
480 remove the influence of internal and external noise from various systems, which will  
481 greatly reduce the accuracy of the observation data.

#### 482 **5.4 Applicability of multiple remote sensing platforms for potential** 483 **geological hazards**

484 The above studies show that there are usually some differences between the  
485 ground-based radar and spaceborne InSAR results of deformation monitoring. These  
486 differences are caused by the observation time period, the observation geometric model  
487 and incidence angle, the deformation reference point, the image ground resolution and  
488 the deformation monitoring accuracy. However, this difference is not due to the large  
489 contradiction between the two technical methods but a reasonable physical  
490 phenomenon, which is a multiangle solution to a problem and is formed by a variety of  
491 physical factors. This finding also reflects the advantages and disadvantages of  
492 spaceborne InSAR and ground-based radar in deformation monitoring of geological  
493 disasters. Therefore, in actual research, the two methods can be combined to form an  
494 effective technical complementary scheme.

495 By combining satellite data and ground-based monitoring technology, the  
496 deformation mechanism and factors influencing geological slopes can be studied from  
497 more perspectives and aspects (Yongsheng Li et al. 2020). Topographic transformations  
498 produced by human disturbances can be recorded by satellite data with high spatial and  
499 temporal resolutions. Due to the limitation of spatial and temporal resolution, the  
500 spaceborne InSAR method is suitable for the early identification and investigation of  
501 the risk of geological hazards. By comparison, ground-based radar is suitable for  
502 geological hazard monitoring, early warning and emergency observation due to its  
503 advantages of higher deformation observation precision, flexible observation angle and  
504 easy deployment (Caduff et al. 2015; Casagli et al. 2010; Nico et al. 2004; Qin et al.  
505 2020). In addition, ground-based radar is the most suitable technique for deformation  
506 observations with high precision in real time to determine the potential of secondary

507 landslides for safety during emergency responses (Antonello et al. 2004; Atzeni et al.  
 508 2015) in the postdisaster phase (Luo et al. 2020). In the case of geological hazards,  
 509 UAVs can be rapidly deployed to capture orthophoto image data to evaluate the  
 510 influence and damage intensities during a disaster for emergency response purposes for  
 511 the first time (Casagli et al. 2017; Nikolakopoulos and Koukouvelas 2017).

512 In recent years, advances in earth observation (EO) from the ground surface,  
 513 aircraft and space have dramatically improved our ability to detect and monitor active  
 514 landslides (Bardi et al. 2014; Dai et al. 2020; Bardi et al. 2016). Various RS platforms,  
 515 including satellites, UAVs, ground-based radar instruments, etc., have been widely  
 516 used in the investigation of geological hazards and in the assessment of disaster  
 517 emergencies. Because the characteristics of each platform differ from those of other  
 518 platforms, different RS platforms may play various roles in different phases of  
 519 landslide hazard evaluations, including the before and after landslide phases. Therefore,  
 520 different platforms and measurement models may have different applications in  
 521 various scenarios and stages of disaster evolution due to their different advantages and  
 522 disadvantages, which can be combined to solve the qualitative investigation and  
 523 quantitative measurement of hidden geological hazards and their deformation  
 524 characteristics. With the support of all these platforms, we can study all elements and  
 525 entire chains of geological disasters. Therefore, satellite-based and ground-based  
 526 observation technologies can effectively complement each other in the time axis and  
 527 deepen the understanding of the development trend of geological hazard deformation  
 528 by constructing the working mechanism of their coordination to provide important  
 529 technical support to prevent risks of major geological disasters. By summarizing nearly  
 530 all RS methods suitable for geological hazard investigation, different features and  
 531 parameters are listed briefly for reference in Table 2 for different scenarios and stages.

532 Table 2 Application characteristics of sky-ground observation technology in geological disaster  
 533 detection

Platform	Advantages	Hazard scene and stage	Application objective	Resolution/Precession	Disadvantages
Optical satellite data	Wide amplitude, multispectral	Early identification of hidden dangers	Trace characteristics survey, disaster risk assessment, large-scale risk census	Submetre	Affected by vegetation cover, affected seriously by weather

Spaceborne InSAR	Wide amplitude, all-weather, all-time	Early identification of hidden dangers	Survey of deformation characteristics, disaster risk assessment, large-scale risk census	Time series: mms; Difference: cms	Long revisit cycle, current dependence on foreign satellites, high-resolution data is expensive
UAV-based tilt photogrammetry	High resolution, 3D modeling, flexible deployment	Disaster investigation, emergency assessment	Trace feature survey, disaster risk verification, disaster assessment	cms	Small imaging width
UAV-SAR	High resolution, all-weather, all-day, flexible deployment	Disaster investigation, emergency assessment	Trace feature survey, disaster risk verification, disaster assessment	cms	UAV-SAR does not support interference processing and has small imaging width
GNSS	High-precision real-time continuous monitoring	Monitoring, forecasting and early warning, emergency monitoring	Deformation characteristics investigation and dynamic monitoring of landslide disaster risk	mms	Sparse points, high observation cost and insufficient remote landslide monitoring
Ground-based radar	All-day, high precision real-time continuous monitoring, can monitor high remote landslides	Monitoring, forecasting and early warning, emergency monitoring	Deformation characteristics investigation and dynamic monitoring of landslide disaster risk	submillimeter	Affected by vegetation and atmosphere, suitable for single landslide monitoring

534

## 535 **6. Conclusion**

536 Based on 656 ground-based radar images collected from September 13-17, 2019,  
537 and 62 spaceborne SAR observations from July 2018 to October 2020, this paper  
538 analyzed the deformation information extraction of an ancient landslide on the right  
539 bank of the Dajinchuan River in Danba County. The maximum deformation area  
540 monitored by ground-based radar is located at the upper part of the continuous curve of  
541 bedrock on the back wall of the ancient landslide, and the maximum deformation is  
542 more than 30 mm. Spaceborne data also measure deformation here, but the measured  
543 maximum deformation area is located in the continuous curved area in the lower part of  
544 the maximum deformation area observed by ground-based radar, and the annual  
545 average deformation rate is more than 40 mm/a.

546 Combined with the local geological topography, meteorological precipitation and  
547 other data, this paper analyzed the main factors affecting the deformation of bedrock in

548 the region, including geological structure factors, topography and geomorphology  
549 factors, hydrological and meteorological conditions, erosion, weathering and human  
550 activities. Additionally, we discussed the reasons for the difference in the deformation  
551 results between the two observation methods and provided suggestions for the scheme  
552 of satellite-ground coobservation. By complementing each other in the time axis, the  
553 effectiveness of spaceborne InSAR in the early identification of geological hazard risks  
554 and the advantages of ground-based radar for the high-precision observation of key  
555 deformation targets were brought into play. The cooperative working mechanism of the  
556 two was more conducive to identifying hidden geological hazards and monitoring risk  
557 sources.

## 558 **References**

- 559 Antonello G, Casagli N, Farina P, Leva D, Nico G, Sieber AJ, et al (2004) Ground-based SAR  
560 interferometry for monitoring mass movements. *Landslides* 1(1):21-8
- 561 Atzeni C, Barla M, Pieraccini M, Antolini F (2015) Early Warning Monitoring of Natural and  
562 Engineered Slopes with Ground-Based Synthetic-Aperture Radar. *Rock Mechanics and Rock*  
563 *Engineering* 48(1):235-46
- 564 Bardi F, Frodella W, Ciampalini A, Bianchini S, Ventisette CD, Gigli G, et al (2014) Integration  
565 between ground based and satellite SAR data in landslide mapping: The San Fratello case study.  
566 *Geomorphology* 223
- 567 Bardi F, Raspini F, Ciampalini A, Kristensen L, Rouyet L, Lauknes TR, et al (2016) Space-Borne and  
568 Ground-Based InSAR Data Integration: The Åknes Test Site. *Remote Sensing* 8(3)
- 569 Caduff R, Schlunegger F, Kos A, Wiesmann A (2015) A review of terrestrial radar interferometry for  
570 measuring surface change in the geosciences. *Earth Surface Processes and Landforms*  
571 40(2):208-28
- 572 Casagli N, Catani F, Ventisette CD, Luzi G (2010) Monitoring, prediction, and early warning using  
573 ground-based radar interferometry. *Landslides* 7(3):291-301
- 574 Casagli N, Frodella W, Morelli S, Tofani V, Ciampalini A, Intrieri E, et al (2017) Spaceborne, UAV and  
575 ground-based remote sensing techniques for landslide mapping, monitoring and early warning.

576            Geoenvironmental Disasters 4(1):9

577    Chen H, Xu Y, Zhuang M, Jiang Z, zhang n (2011) Study on the construction of geological disaster  
578            emergency support system. The Chinese Journal of Geological Hazard and Control (04):108-11

579    Chen T (2020) Deformation monitoring of ground-based InSAR based on TCPInSAR technology.  
580            China University of Geosciences (Beijing)

581    Dai K, Peng J, Zhang Q, Wang Z, Liu X (2020) Entering the Era of Earth Observation-Based Landslide  
582            Warning Systems: A Novel and Exciting Framework. IEEE Geoscience and Remote Sensing  
583            Magazine PP(99)

584    Donnarumma A, Revellino P, Grelle G (2013) Guadagno FM Slope Angle as Indicator Parameter of  
585            Landslide Susceptibility in a Geologically Complex Area. Landslide Science and Practice

586    Duan A, Xiao Z, Wu G (2016) Characteristics of Climate Change over the Tibetan Plateau Under the  
587            Global Warming During 1979-2014. Climate Change Research 12(5)

588    Li B, Li Y, Jiang W, Cai J, Gan J (2019) Research and Application of Slope Dynamic Monitoring Based  
589            on Ground-Based Real Aperture Radar. Geomatics and Information Science of Wuhan University  
590            44(007):1093-8

591    Li M, Zheng W, Shi S, Xie Z (2008) The revival mechanism and stability analysis to Jiaju Landslide of  
592            Danba County in Sichuan Province. Journal of mountain science (05):69-74

593    Li Y, Jiao Q, Hu X, Li Z, Li B, Zhang J, et al (2020) Detecting the slope movement after the 2018  
594            Baige Landslides based on ground-based and space-borne radar observations. International  
595            Journal of Applied Earth Observation and Geoinformation 84(C)

596    Li Y, zhang J, Li Z, Luo Y (2013) Land Subsidence in Beijing City from InSAR Time Series Analysis  
597            with Small Baseline Subset. Geomatics and Information Science of Wuhan University  
598            38(011):1374-7

599    Lu H, Li W, Xu Q, Dong X, Dai C, wang D (2019) Early Detection of Landslides in the Upstream and  
600            Downstream Areas of the Baige Landslide, the Jinsha River Based on Optical Remote Sensing and  
601            InSAR Technologies. Geomatics and Information Science of Wuhan University 44(9):1342-54

602    Luo Y, Jiang W, Li B, Jiao Q, Li Y, Li Q, et al (2020) Analyzing the formation mechanism of the  
603            Xuyong landslide, Sichuan province, China, and emergency monitoring based on multiple remote  
604            sensing platform techniques. Geomatics, Natural Hazards and Risk 11(1):654-77

605    Nico G, Leva D, Antonello G, Tarchi D (2004) Ground-based SAR interferometry for terrain mapping:

606 Theory and sensitivity analysis. IEEE Transactions on Geoscience and Remote Sensing  
607 42(6):1344-50

608 Nie B (2018) Landslide Deformation Detection and Identification Based on InSAR Technology—a  
609 Case of Danba County. Chengdu University of Technology

610 Nikolakopoulos KG, Koukouvelas I (2017) Emergency response to landslide using GNSS  
611 measurements and UAV. Earth Resources & Environmental Remote Sensing/gis Applications

612 Qin H, Ma H, Yu Z (2020) Analysis Method of Landslide Early Warning and Prediction Supported by  
613 Ground-Based SAR Technology. Geomatics and Information Science of Wuhan University  
614 v45(11):50-9

615 Wang Z, Li Z, Liu Y, Peng J, Mills J (2019) A New Processing Chain for Real-Time Ground-Based  
616 SAR (RT-GBSAR) Deformation Monitoring. Remote Sensing 11(20):2437-

617 Wang Z, Li Z, Mills J (2019) Modelling of instrument repositioning errors in discontinuous  
618 Multi-Campaign Ground-Based SAR (MC-GBSAR) deformation monitoring. ISPRS Journal of  
619 Photogrammetry and Remote Sensing 157:26-40

620 Wu X, Ma H, zhang J (2019) Development status and application of Ground-Based Synthetic Aperture  
621 Radar. Geomatics and Information Science of Wuhan University 044(007):1073-81

622 Xu Q (2020) Understanding and Consideration of Related Issues in Early Identification of Potential  
623 Geohazards. Geomatics and Information Science of Wuhan University 45(11):1651-9

624 Zhang L, Liao M, Dong J, Xu Q, Gong J (2018) Early Detection of landslide hazards in mountainous  
625 areas of West China using time series SAR interferometry-A case study of Danba, Sichuan.  
626 Geomatics and Information Science of Wuhan University 043(012):2039-49

627 Zhang X, Yang H, Jiang J, Peng J, Xu J (2017) GB-InSAR atmospheric delay for highly coherent  
628 points correction. Science of Surveying and Mapping 042(001):53-8  
629

# Figures

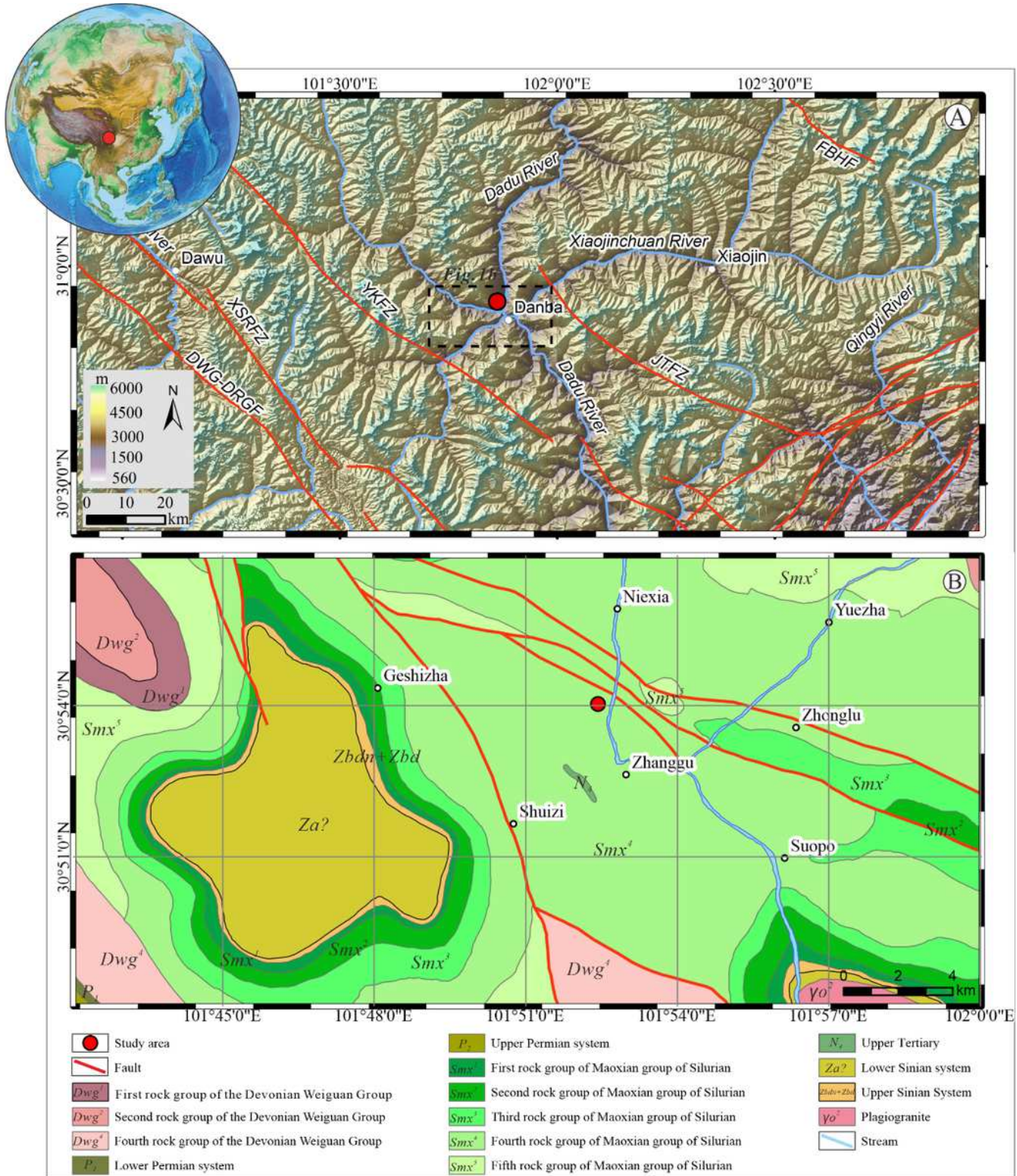
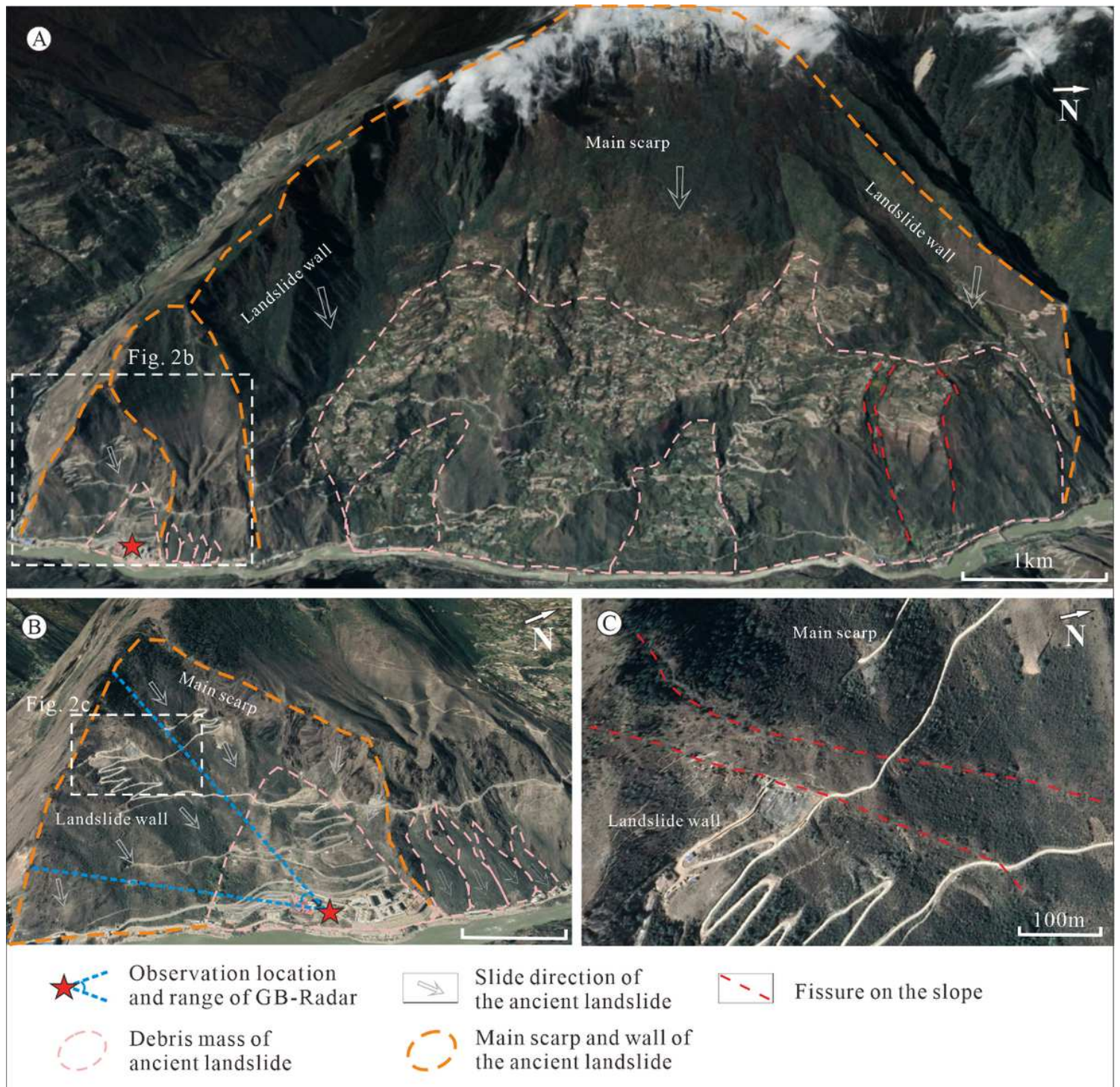


Figure 1

(a) Regional hillshade map of the study area. A Shuttle Radar Topography Mission (SRTM) hillshade map is used as the base map. (b) Regional geological setting surrounding the study area (China Geological Survey, 2014). The red line denotes the main faults in this region. YKFZ: Yuke fault zone; JTFZ: Jintang

arc fault; XSHFZ: Xianshui River fault; DWG-GRGF: Dawagou-Dourigou fault; and FBHF: Fubian River fault. Note: The designations employed and the presentation of the material on this map do not imply the expression of any opinion whatsoever on the part of Research Square concerning the legal status of any country, territory, city or area or of its authorities, or concerning the delimitation of its frontiers or boundaries. This map has been provided by the authors.



**Figure 2**

Geographic location map. (a) The whole picture of the Jiaju landslide group. (b) The location and range of ground-based radar. (c) The surface fissure on the slope. Note: The designations employed and the

presentation of the material on this map do not imply the expression of any opinion whatsoever on the part of Research Square concerning the legal status of any country, territory, city or area or of its authorities, or concerning the delimitation of its frontiers or boundaries. This map has been provided by the authors.

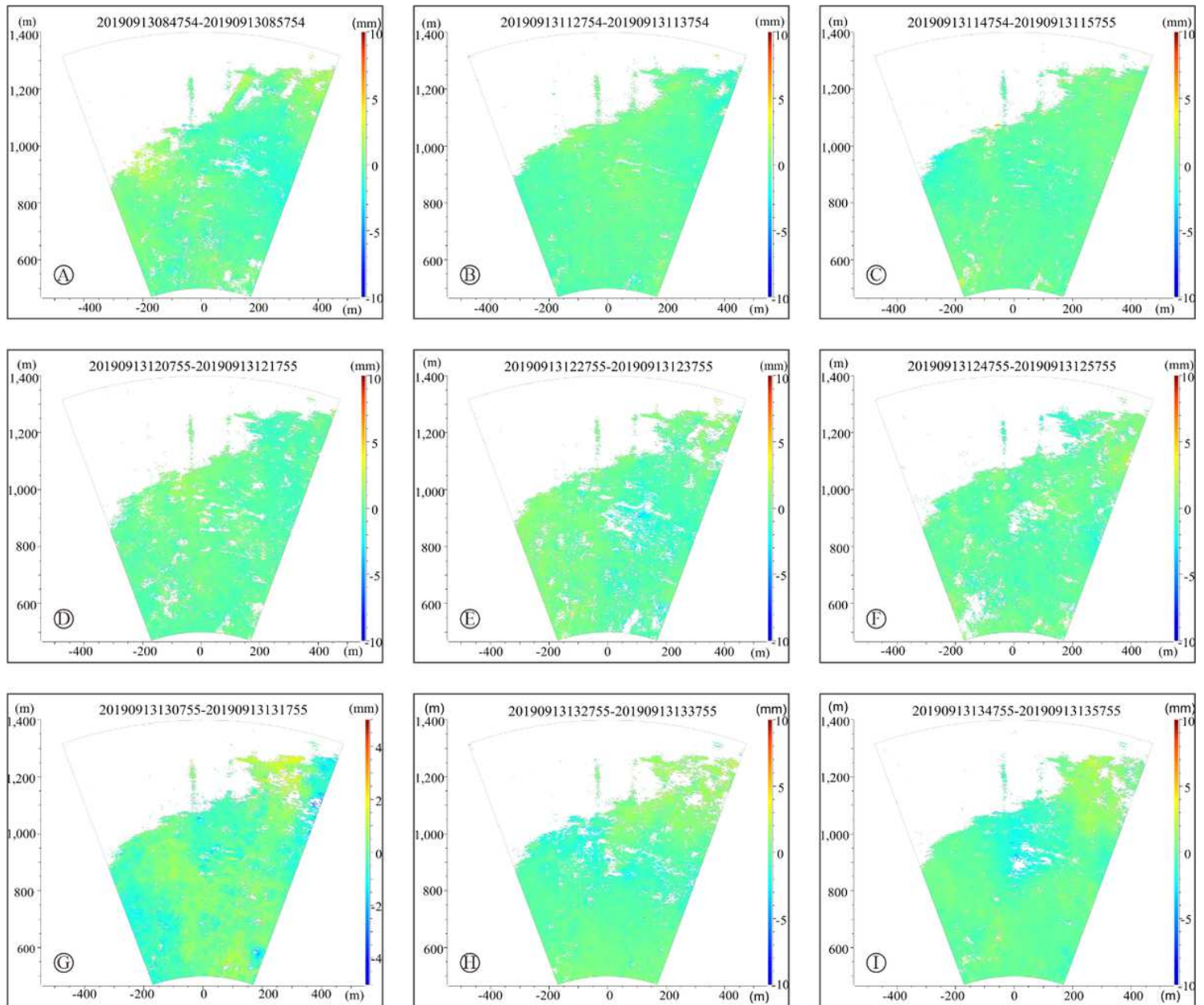


**Figure 3**

Examples of differential interferograms generated during the processing of ground-based radar data. The two numbers in the upper part of each figure denote the observation dates of two data points used to generate the differential interferogram. 20190913084754-20190913085754 denotes the differential interferogram generated between two data points observed at 8 h 47 m 54 s on September 13, 2019, and at 8 h 57 m 54 s on September 13, 2019. The origin point of the coordinate system is the position of the ground-based radar.

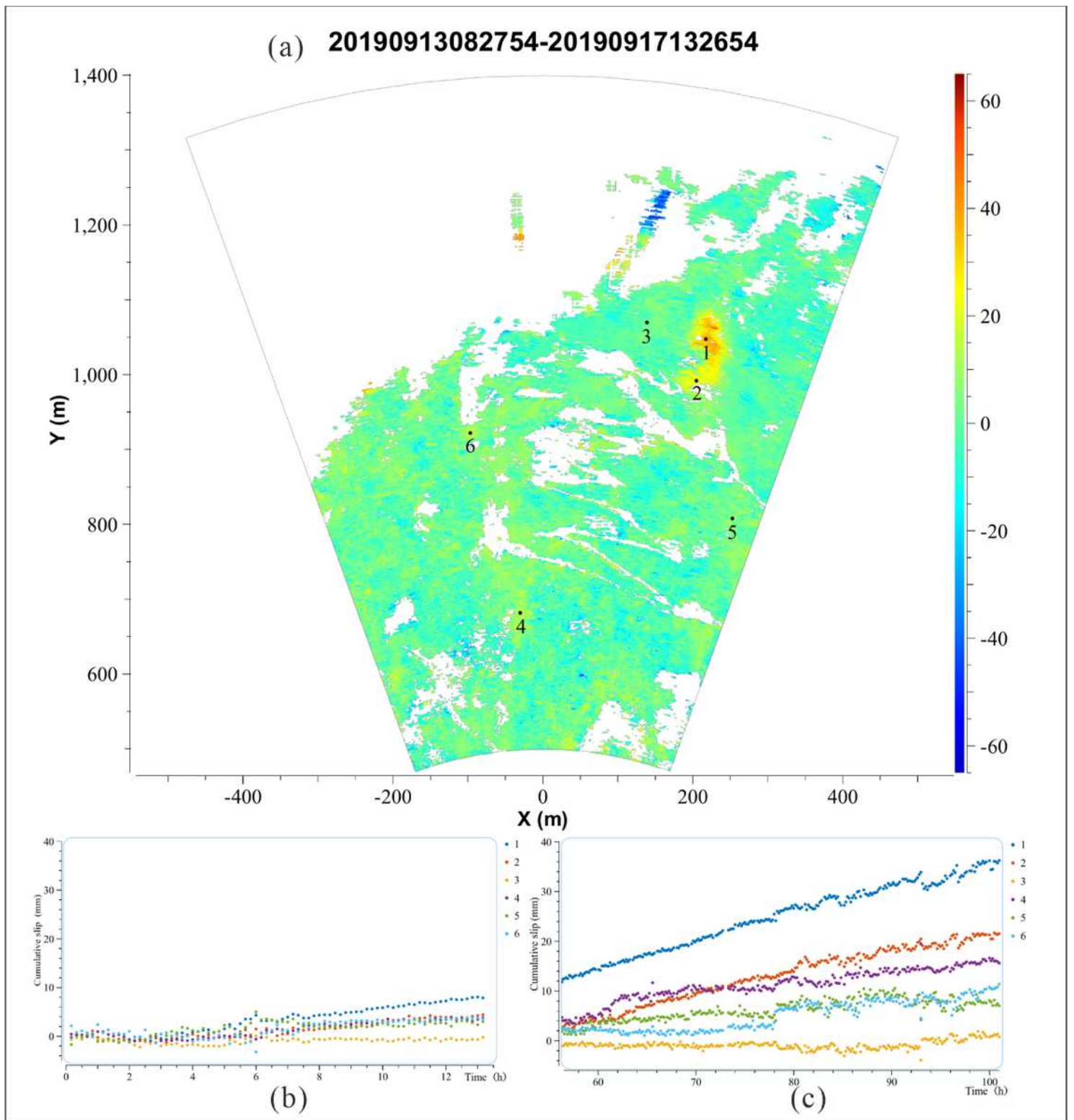


**Figure 4**

(a) Cumulative slips of the slope deformation along the LOS direction measured by the ground-based radar device. The number at the top of the figure represents the time when ground-based radar began and ended observations, that is, the observation time range of the cumulative deformation map generated; and 20190913082754-20190917132654 represents ground-based radar observation time from 8:27:54 on September 13, 2019 to 13:26:54 on September 17, 2019. The origin of the coordinates represents the

position of the ground-based radar. (b) and (c) are the results of the accumulated deformation of the selected points in the time series of 0~13.5 h and 56~101 h, respectively.

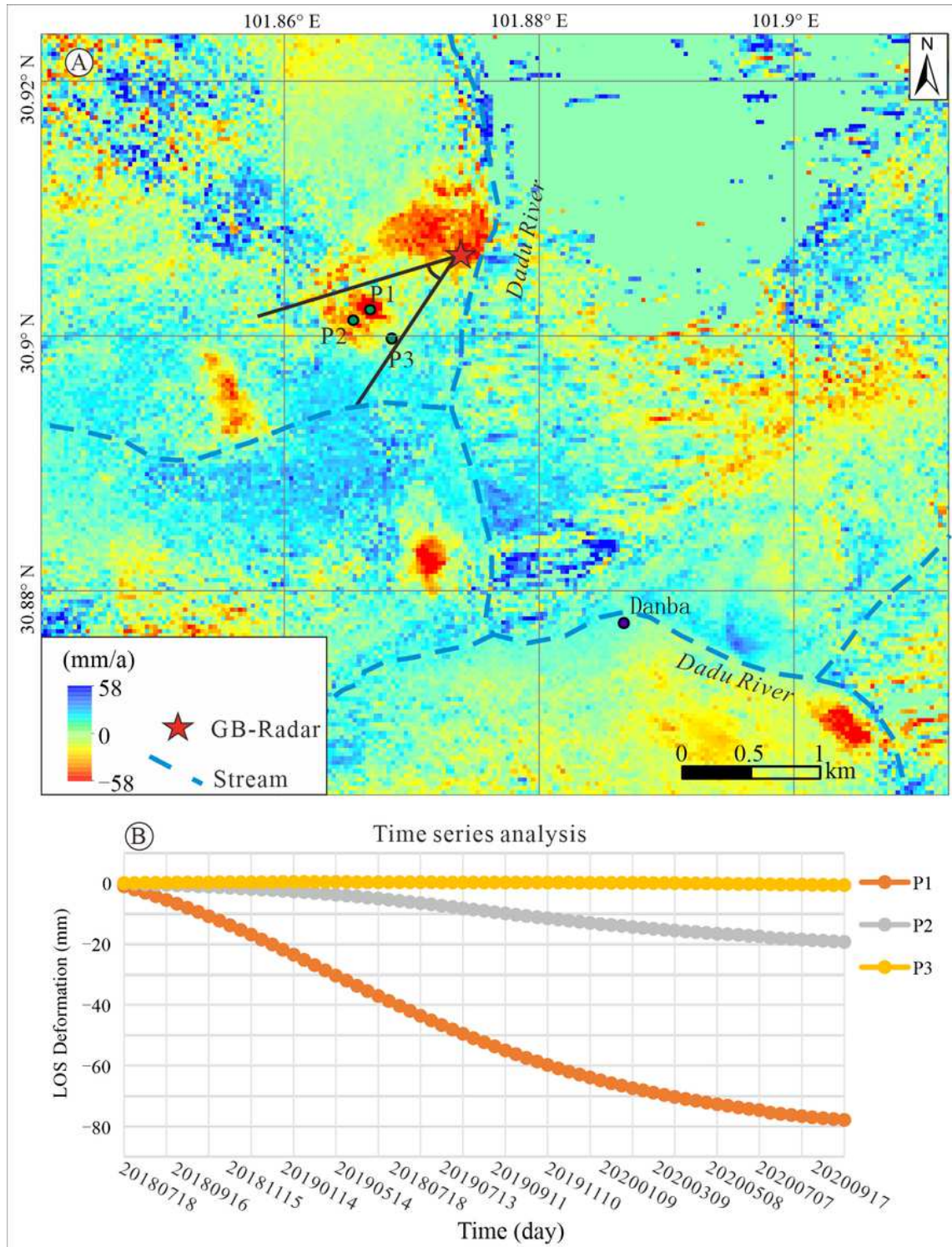


**Figure 5**

(a) Regional annual deformation rate map measured by Sentinel-1 data, and P1, P2 and P3 are the three points selected in the observation area of ground-based radar. The gray line is the scanning angular scope of ground-based radar. (b) The line-of-sight cumulative deformation map of three selected points

P1, P2 and P3 in the study area. Note: The designations employed and the presentation of the material on this map do not imply the expression of any opinion whatsoever on the part of Research Square concerning the legal status of any country, territory, city or area or of its authorities, or concerning the delimitation of its frontiers or boundaries. This map has been provided by the authors.

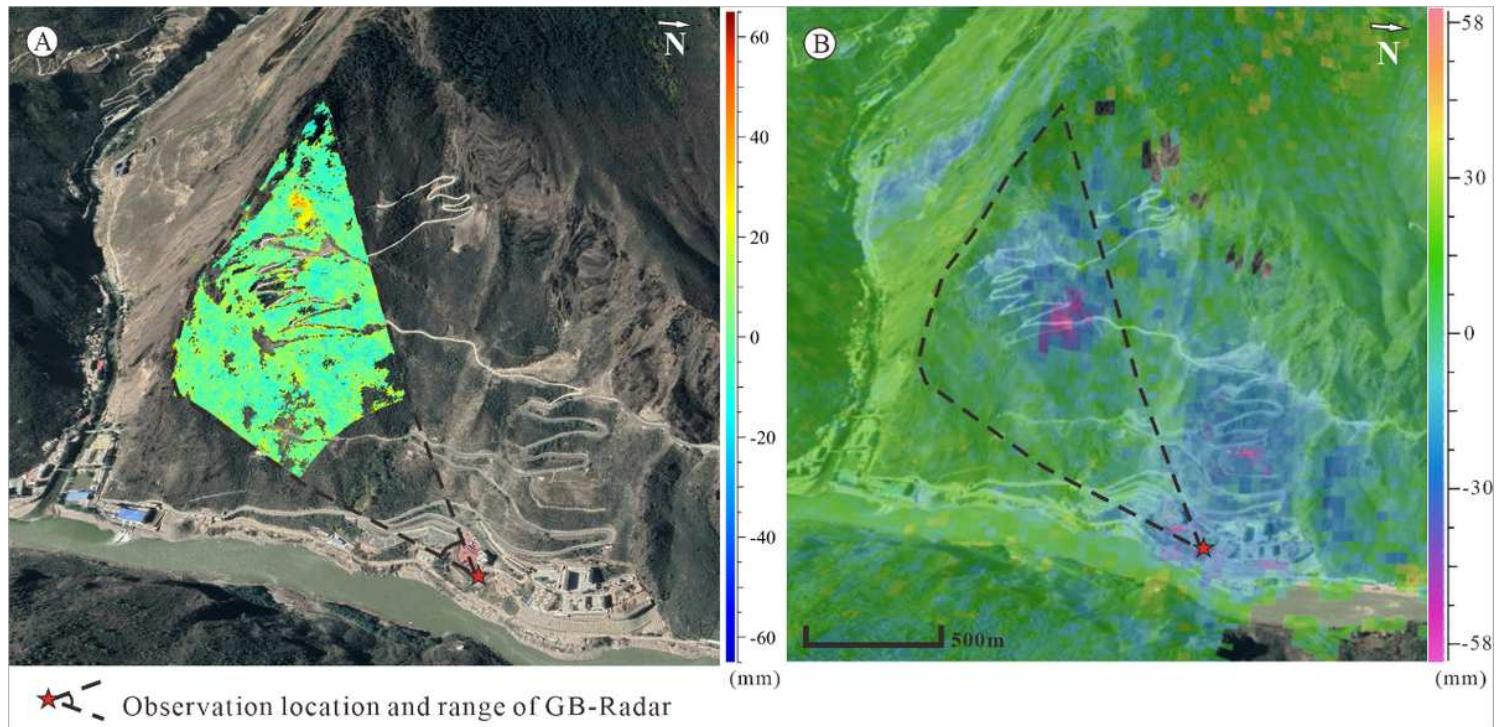


**Figure 6**

(a) Map of ground-based radar monitoring results superimposed on Google Earth; (b) Map of Sentinel 1 monitoring results superimposed on Google Earth. Note: The designations employed and the presentation of the material on this map do not imply the expression of any opinion whatsoever on the part of Research Square concerning the legal status of any country, territory, city or area or of its authorities, or concerning the delimitation of its frontiers or boundaries. This map has been provided by the authors.



**Figure 7**

Sketch map of the slope and angle of the study area Note: The designations employed and the presentation of the material on this map do not imply the expression of any opinion whatsoever on the part of Research Square concerning the legal status of any country, territory, city or area or of its authorities, or concerning the delimitation of its frontiers or boundaries. This map has been provided by the authors.

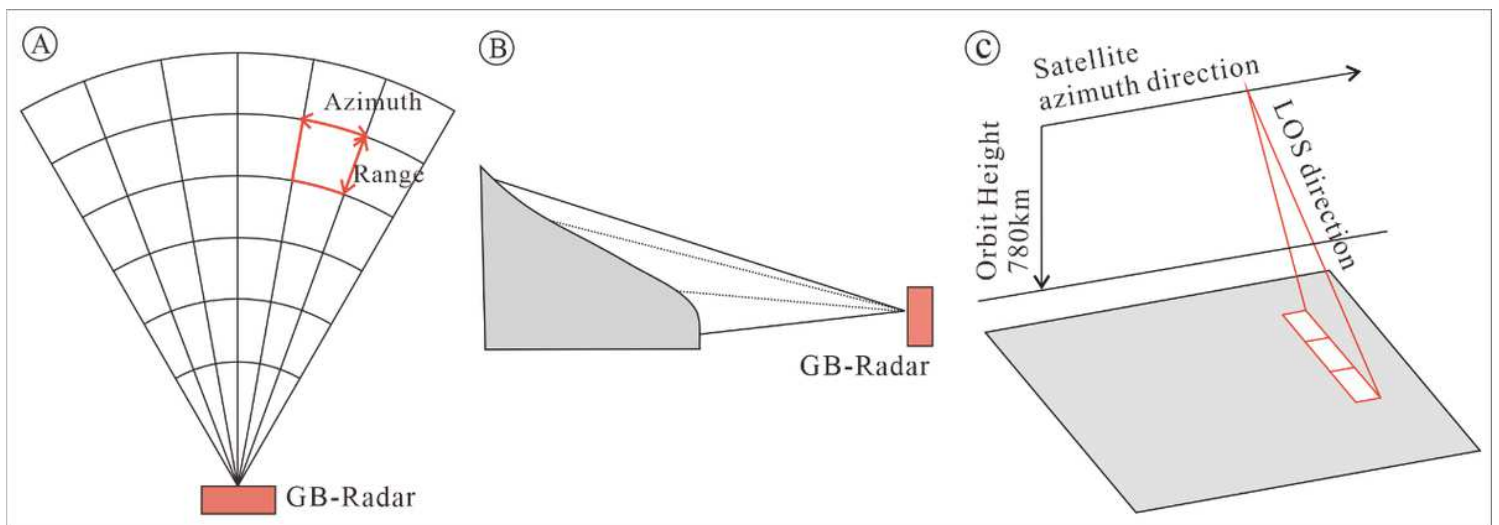


**Figure 8**

(a) Ground-based radar monitoring plan sketch (b) Ground-based radar monitoring profile sketch (c) A schematic of the Sentinel-1 imaging mode